

# Epidemiological Model Calibration via Graybox Bayesian Optimization

Puhua Niu, Byung-Jun Yoon, *Senior Member IEEE*, and Xiaoning Qian, *Senior Member IEEE*

**Abstract**—In this study, we focus on developing efficient calibration methods via Bayesian decision-making for the family of compartmental epidemiological models. The existing calibration methods usually assume that the compartmental model is *cheap* in terms of its output and gradient evaluation, which may not hold in practice when extending them to more general settings. Therefore, we introduce model calibration methods based on a “graybox” Bayesian optimization (BO) scheme, more efficient calibration for general epidemiological models. This approach uses Gaussian processes as a surrogate to the expensive model, and leverages the functional structure of the compartmental model to enhance calibration performance. Additionally, we develop model calibration methods via a decoupled decision-making strategy for BO, which further exploits the decomposable nature of the functional structure. The calibration efficiencies of the multiple proposed schemes are evaluated based on various data generated by a compartmental model mimicking real-world epidemic processes, and real-world COVID-19 datasets. Experimental results demonstrate that our proposed graybox variants of BO schemes can efficiently calibrate computationally *expensive* models and further improve the calibration performance measured by the logarithm of mean square errors and achieve faster performance convergence in terms of BO iterations. We anticipate that the proposed calibration methods can be extended to enable fast calibration of more complex epidemiological models, such as the agent-based models.

**Index Terms**—Compartmental Model, Bayesian Optimization, Model Calibration, Gaussian Process, Knowledge Gradient

## I. INTRODUCTION

**P**ANDEMICS like the recent coronavirus disease (COVID-19) have shown enormous impacts on public health worldwide. The development of computational epidemiological models is crucial for gaining better quantitative understanding of the disease spread and enabling swift decision-making to design effective mitigation strategies. In fact, well-calibrated epidemiological models can serve as a useful guide for forecasting and quantifying the epidemic risk and implementing effective public health measures to control the spread of epidemic diseases [2], [9].

This work was supported in part by the U.S. Department of Energy (DOE) Office of Science under Award KJ0403010/FWP CC132.

Puhua Niu is with the Department of Electrical & Computer Engineering, Texas A&M University, College Station, TX 77843 USA.

Byung-Jun Yoon is with the Department of Electrical & Computer Engineering, Texas A&M University, College Station, TX 77843 USA; the Computational Science Initiative, Brookhaven National Laboratory, Upton, NY 11973 USA.

Xiaoning Qian is with the Department of Electrical & Computer Engineering, Texas A&M University, College Station, TX 77843 USA; the Department of Computer science & Engineering, Texas A&M University, College Station, TX 77843 USA; the Computational Science Initiative, Brookhaven National Laboratory, Upton, NY 11973 USA (e-mail: xqian@ece.tamu.edu).

Compartmental models, such as the commonly adopted SIR (Susceptible-Infectious-Recovered) model, constitute an important family of population-based epidemiological models. Models in this family take the form of Ordinary Differential Equation (ODE) systems that capture the general trends and dynamics in the subpopulations represented by different compartments. In this work, we focus on this family of models while considering a new “Quarantined” state represented by an additional compartment. This new state aims at better mimicking the dynamic trajectories of the epidemic spreads, typical in airborne diseases such as seasonal flu and COVID-19, resulting in a four-compartment SIQR model [25].

To accurately model real-world physical processes, it is crucial for computer models to fine-tune their model parameters based on observed data to capture inherent attributes of the physical processes, which can not be directly or easily measured by means of physical experiments. For instance, material properties, such as porosity and permeability are important computer inputs in computational material simulations, which cannot be measured directly in physical experiments. In the applied mathematics and computational science literature, the methods used to identify those parameters are called model calibration techniques and the resulting parameters are called calibration parameters [22], [28]. The basic idea of calibration is to find the combination of the calibration parameters, under which the simulated computer outputs align with the observed physical data. A well-calibrated SIQR model may allow people to make more accurate predictions of pandemic risk and enable them to make better-informed decisions on how to mitigate.

The existing method often assumes that the computer model is *cheap* [33]. This means that: the explicit form of the optimization objective  $f(x)$  for calibration parameters  $x$  is known and we can evaluate the first- or second-order derivatives of  $f(x)$  with respect to (w.r.t.)  $x$ . For an ODE system, deriving the explicit form of  $f(x)$  and  $\nabla_x f(x)$  can be infeasible when the ODE is non-linear. Recent advances show that sensitivity analysis allows us to evaluate the gradient  $\nabla_x f(x)$  and perform the gradient-descent optimization method for the estimation of  $x$  [13], [19]. Correspondingly, physics-informed machine learning [21] is drawing increasing attention as it integrates data and mathematical models into deep neural networks or other regression models by enforcing fundamental physical laws.

In real-world scenarios when calibrating a computer simulation software, we are usually blind to the explicit forms of both  $f(x)$  and  $\nabla_x f(x)$  and we may be able to access only the output of  $f(x)$ . We classify this type of computer model as

*expensive*. Besides, even if we know the explicit form of  $f(x)$  and  $\nabla_x f(x)$ , there are usually some key hyper-parameters  $x'$ , which are fixed during gradient-based optimization. Given  $x$ , the explicit form of  $f_{x'}$  is intractable in most cases. Therefore,  $f_{x'}$  can also be classified as *expensive*. Hence, it is valuable to pay attention to the calibration problem for such *expensive* computer models. Bayesian Optimization (BO) is one conventional approach for such scenario when evaluating  $f(x)$  is expensive, where we use a surrogate model to approximate  $f(x)$  and the optimization process is sequential. In each BO round, we make a *Bayesian decision* so that some expected utility is maximized and then the corresponding output is queried from the computer model based on this decision to refine the surrogate model to guide the optimization of the objective function  $f(x)$  [15], [18].

This paper concentrates specifically on the calibration of the SIQR model based on BO and is organized as follows. First, we explain the configurations of the SIQR model and the model calibration setup. Then we introduce our calibration methods based on a “graybox BO” approach, instead of the usual “blackbox BO”, where the experts’ prior knowledge about the computer models is integrated into the BO formulation to improve its optimization performance. Finally, we explain how the graybox BO works for decoupled decision-making, accompanied by a new acquisition function. In our experiments, we evaluate the performance of our proposed graybox BO-based model calibration methods and compare them with traditional blackbox BO-based implementations to demonstrate the benefits of integrating prior model knowledge into the calibration process.

## II. PRELIMINARIES

### A. SIQR model

In this model, people in a given population are classified into four compartments: *Susceptible (S)*, *Infectious (I)*, *Recovered (R)*, and *Quarantined (Q)*. Those who have not been infected are considered susceptible. Transmission occurs between susceptible and infected individuals. The number of symptomatic patients, equivalent to the number of infected individuals, decreases through treatment and/or quarantine. Recovered individuals are assumed to remain immune to further infection. Therefore, all people will be in the recovered group after an adequate period. The dynamics of the SIQR model are given by the following set of ordinary differential equations (ODEs) [25]:

$$\begin{cases} \nabla_t S(t) = & -\beta(t)S(t) \\ \nabla_t I(t) = & \beta(t)S(t) - \lambda(t)I(t) - \gamma I(t) \\ \nabla_t R(t) = & \gamma I(t) + \delta Q(t) \\ \nabla_t Q(t) = & \lambda(t)I(t) - \delta Q(t) \end{cases} \quad (1)$$

where  $S(t)$ ,  $I(t)$ ,  $Q(t)$  and  $R(t) \in [0, N]$  are the populations of compartments ‘S’, ‘I’, ‘Q’ and ‘R’ respectively. It can be verified that the ODEs guarantee the conservation of the population,  $S(t) + I(t) + Q(t) + R(t) = N$ . A schematic illustration of such an SIQR model is shown in Figure 1. We note that there are many compartmental epidemiological models based

on different extensions of the original SIR model [11], [26]. While we focus on SIQR model calibration in this paper, the presented model calibration methods can be applied to all these variants in a straightforward manner. More importantly, calibration of more complicated epidemiology models based on agent-based models (ABMs) can also leverage our proposed methods if their critical parameters can be identified, where calibration efficiency is even more important due to their significantly higher computational complexity compared to the ODE-based compartmental models [1], [4], [10].

### B. Model Calibration

Most of the existing calibration methods [12], [14], [29], [31], [32], [34] follow or adapt from the Bayesian approach pioneered by Kennedy and O’Hagan (KOH) [22]. In practice, we can only collect epidemiological data in the occurrence of an epidemic. In other words, we can observe the population’s dynamic trajectory *only once*, making model calibration more challenging than in other statistical inference or machine learning tasks. Supposing one such trajectory with time length  $T$  are observed, we denote the observed epidemiological data as  $\{\mathbf{d}^t = (d_1^t, \dots, d_4^t)\}_{t=1}^T$  and make the following assumption:

$$\mathbf{d}^t = \zeta^t + \epsilon \approx \eta^t(x) + \epsilon, \quad (2)$$

where  $\zeta$  is the unknown ground-truth underlying epidemic process,  $\eta$  is a computer model (e.g., SIQR model) that we would like to calibrate to simulate the behavior of  $\zeta$  and fit the observed epidemiological data,  $x \in \mathbb{R}^D$  is the  $D$ -dimensional *calibration* parameter vector of  $\eta$ , and  $\epsilon \sim \mathcal{N}(0, \text{Diag}(\mathbf{1}))$  represents the observation noise. In this work,  $\eta^t(x) = (\eta_1^t(x), \eta_2^t(x), \eta_3^t(x), \eta_4^t(x)) = (S(t; x), I(t; x), Q(t; x), R(t; x))$  corresponds to the output of the SIQR model with  $x$  representing parameters of rate functions  $\{\beta(t; x), \gamma(t; x), \delta(x), \gamma(x)\}$ . By our assumption,  $d^t | \eta^t(x) \sim \mathcal{N}(\eta^t(x), 1)$ , and the Maximum Log-likelihood Estimation (MLE) of  $x$  corresponds to [31], [33]:

$$\begin{aligned} x^* &= \operatorname{argmax}_x \sum_t^T g(\eta^t(x)), \\ g(\eta^t(x)) &:= -\frac{1}{T} \sum_{i=1}^4 (d_i^t - \eta_i^t(x))^2, \end{aligned} \quad (3)$$

where  $g$  denotes the likelihood function as the negative Square Error (SE) function based on the Gaussian assumption. For notation compactness, we denote  $g(\eta^t(x))$  as  $f^t(x)$ . The goal of model calibration is the maximization of the corresponding negative Mean Square Error (MSE),  $\sum_t f^t(x)$ .

## III. METHODOLOGY

Instead of following the traditional KOH Bayesian model calibration scheme [22], we resort to a new model calibration framework leveraging Bayesian Optimization (BO) [18]. Under this framework, model calibration is formulated into the optimization of the correspondingly designed utility function, called *acquisition function*. In BO, Gaussian Processes (GPs)

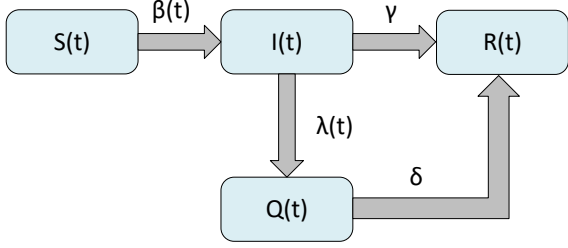


Fig. 1: Diagram depicting an SIQR compartmental epidemiological model. Each arrow indicates that the population rise of the ending compartment is caused by the population decrease of the starting compartment.

have been typically used as cheap surrogates of  $f(x)^1$ . In this way, we circumvent the difficulties in optimizing  $f(x)$  directly. To be more specific, the standard BO approach treats  $f(x)$  as a blackbox function and starts modeling it by a set of GP prior distributions,  $\mathcal{N}(\mu(x), \Sigma(x))$ . Then, it iteratively chooses the next point at which to evaluate  $f$  with the procedure described as follows.

Given  $n$  observations of the objective function customized for model calibration,  $f(x^1), \dots, f(x^n)$ , we first infer the posterior distribution,  $\mathcal{N}(\mu_n(x), \Sigma_n(x))$ , which conditions on the  $\{f(x^l), x^l\}_{l=1}^n$ . Then, this posterior distribution is used to compute an acquisition function. Finally, we make a *Bayesian decision* that chooses the next point to be evaluated,  $x^{n+1}$ , as the point that maximizes this acquisition function. After  $N$  iteration, the candidates  $x^{best} = \operatorname{argmax}_x \mu_N(x)$  is the calibrated parameter choice.

#### A. Graybox BO

It is clear that given the simulated dynamics  $\eta(x)$ , evaluation of the model calibration performance metric  $g$  is cheap and does not need to be approximated. Instead of directly modeling  $f(x)$  as a blackbox objective function as typically done in BO, for SIQR model calibration, we here first use a set of GPs, denoted by  $\mathbf{y}(x)$ , as the surrogate to  $\eta(x)$ . With that, we then model  $f(x)$  as a graybox objective, by a *Composite Function (CF)* [5]:

$$g(\mathbf{y}(x)) = \frac{1}{T} \sum_i (d_i - y_i(x))^2. \quad (4)$$

Spared from the modeling of  $g$ , the model calibration performance can be expected to be further improved. Furthermore, as shown in Figure 1, the workflow of the SIQR model encompasses a set of input-output structures between functions of each compartment. For example, infectious population ‘I’ are exclusively transferred from susceptible population ‘S’, and individuals in the recovery compartment ‘R’ only come from compartments ‘I’ and ‘Q’. Therefore, one may expect

<sup>1</sup>In the following text, we will consider the maximization of the acquisition function  $f^t(x)$  instead of  $\sum_t f^t(x)$  for notation compactness, and omit the subscript  $t$ , where it does not introduce ambiguity.

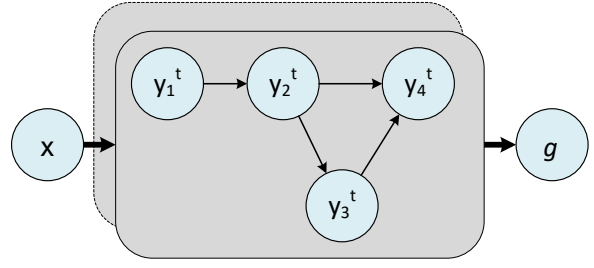


Fig. 2: Function network structure of the SIQR model calibration, where the two bold arrows indicate that  $x$  and  $g$  are the parent node and child node of  $y_{1:4}$  respectively.

that leveraging these functional structures may lead to improved calibration performance. Integrating these relationships into the BO method gives rise to a *Function Network (FN)*,  $\mathcal{G}(\mathcal{V}, \mathcal{E})$ , as shown in Figure 2. In the graph, the set of nodes  $\mathcal{V} = \{v | y_1, \dots, y_4, x, g\}$  denote four GP sets associated with the four compartments ‘S’, ‘I’, ‘Q’ and ‘R’ respectively, calibration parameters  $x$ , and performance metric  $g$ . The graph also contains a set of edges  $\mathcal{E} = \{(v \rightarrow v') | v, v' \in \mathcal{V}\}$ , where  $(v \rightarrow v')$  means node  $v'$  takes the output of nodes  $v$  as its input [6]. Suppose we already have made queries from the computer model  $\eta$  by simulating trajectories of subpopulations in each compartment at different settings and obtain  $\mathcal{D}_n = \{\hat{\mathbf{y}}^l = \eta(x^l), x^l\}_{l=1}^n$  at  $n$  calibration parameter vectors. We have:

$$P_n(\mathbf{y}(x)) = \prod_{i=1}^4 P_n(y_i(x), Pa_i), \quad (5)$$

$$y_i \sim \mathcal{N}(\mu_n^i(x, Pa_i), \sigma_n^i(x, Pa_i)),$$

where  $Pa_i = \{y_j : (y_j \rightarrow y_i) \in \mathcal{E}\}$  denotes the GPs that are the parent nodes of  $y_i$  in graph  $\mathcal{G}$ ,  $P_n(y_i(x), Pa_i) = P(y_i(x), Pa_i | \hat{\mathbf{y}}^{1:n}(x^{1:n}))$  denotes the posterior distribution of GP  $y_i$  with mean  $m_n^i$  and variance  $\sigma_n^i$ . Given  $\mathcal{D}_n$ , we choose the GP prior  $P(y_i^{1:n}(x^{1:n}), Pa_i^{1:n})$  to be multivariate normal with a Matérn covariance kernel and a constant mean, whose hyper-parameters are obtained by MLE over  $P(\hat{y}_i^{1:n}(x^{1:n}), \widehat{Pa}_i^{1:n})$ . Then we infer the posterior from  $P(\hat{y}_i^{1:n}(x^{1:n}), \widehat{Pa}_i^{1:n}, y_i(x, Pa_i))$  [16].

Taking the Knowledge Gradient (KG) [16], [17], a typical formulation of acquisition functions as an example, we define the graybox acquisition function according to the FN as:

$$\alpha_n(x) = \mathbb{E}_{P_n(\mathbf{y}(x))} [u_{n+1}^*(\mathbf{y}, x)] - u_n^* \quad (6)$$

where  $u_n^* = \max_x u_n(x)$ ,  $u_n(x) = \mathbb{E}_{P_n(\mathbf{y}(x))} [g(\mathbf{y})]$ ,  $u_{n+1}^*(\mathbf{y}(x)) = \max_{x'} u_{n+1}(x'; \mathbf{y}(x))$ , and  $u_{n+1}(x'; \mathbf{y}(x)) = \mathbb{E}_{P_{n+1}(\mathbf{y}'(x'); \mathbf{y}(x))} [g(\mathbf{y}')]$ . On the right-hand side of the formula above, the second term is the largest expected metric value based on the current GPs, and the first term is the largest expected metric value if the GPs are further conditioned

on predicted data  $(\mathbf{y}(x), x)$ . In comparison, the expectations  $\mathbb{E}_{P_n}[\mathbf{y}]$  and  $\mathbb{E}_{P_{n+1}}[\mathbf{y}]$  are computed in the original KG.

Due to the maximization operator within the expectation, neither the original nor graybox versions of KG can be computed explicitly. Thus, we resort to Monte Carlo estimation [3] of the expectations and the reparametrization trick [23], so that  $\hat{\alpha}$  is an unbiased estimation of  $\alpha$  and  $\nabla_x \hat{\alpha}$  is feasible. To be more specific, we estimate the acquisition function via:

$$\hat{\alpha}(x) = \frac{1}{K} \sum_{k=1}^K \hat{u}_{n+1}^*(x, \hat{\mathbf{y}}^{(k)}(x)) - \hat{u}_n^*,$$

$$\hat{u}_{n+1}^*(x, \hat{\mathbf{y}}^{(k)}(x)) = \max_{x'} \frac{1}{L} \sum_{l=1}^L g(\hat{\mathbf{y}}'_{(l,k)}(x'; x)),$$

$$\hat{u}_n^* = \max_{x''} \frac{1}{L} \sum_{l=1}^L g(\hat{\mathbf{y}}''_{(l)}(x'')),$$

$$\hat{y}_{i,(k)}(x) = \mu_n^i(x, \widehat{P}a_{i,(k)}(x)) + \sigma_n^i(x, \widehat{P}a_{i,(k)}(x)) \hat{\epsilon}_i^{(k)}$$

$$\begin{aligned} \hat{y}'_{i,(l,k)}(x'; x) &= \mu_{n+1}^i(x', \widehat{P}a'_{i,(l,k)}(x'; \hat{\mathbf{y}}^{(k)}(x))) \\ &\quad + \sigma_{n+1}^i(x', \widehat{P}a'_{i,(l,k)}(x'; \hat{\mathbf{y}}^{(k)}(x))) \hat{\epsilon}_i^{(l,k)} \end{aligned}$$

$$\hat{y}''_{i,(l)}(x'') = \mu_n^i(x'', Pa''_{i,(l)}(x'')) + \sigma_n^i(x'', Pa''_{i,(l)}(x'')) \hat{\epsilon}_i^{(l)}, \quad (7)$$

where  $\hat{\epsilon}_i$  denotes a sample of  $\epsilon_i \sim \mathcal{N}(0, 1)$ ,  $K = 8$ , and  $L = 128$ . The computational cost for inferring  $P_n$  is about  $\mathcal{O}(n^3)$  and does not scale up with the dimension of GPs' input (i.e.,  $x$  or  $[x, Pa_i]$ ) [30]. Thus, the computational complexity of the original and graybox versions of KG are similar. The workflow of our calibration method based on graybox BO is illustrated in Figure 3 with the pseudo-code summarized in Algorithm 1.

### B. Decoupled Decision-Making

In practice, epidemiological data  $\mathbf{d}$  from the unknown epidemic process  $\zeta$  may not be observed at synchronized time points. In other words, some observations at the corresponding time point may be missing in practice. For example, when  $d = \{\emptyset, d_2, d_3, d_4\}$ , where  $d_1$  is missing in the observed data, we may only be able to compute  $g(\mathbf{y}(x)) = \frac{1}{T} \sum_{i \neq 1} (y_i(x) - d_i)^2$ . In such a scenario of *decoupled* observations, the function network organization of GPs allows us to infer the function form  $y_1(x)$  by leveraging the ground-truth functional dependency represented by  $\mathcal{G}$ . To be more specific,

$$g \not\perp v, \quad \forall v \in \text{An}_g, \quad (8)$$

where  $v \not\perp v'$  indicates that  $v$  and  $v'$  are statistically dependent so that  $P(v|v') \neq P(v)$  for any two random variables  $v$  and  $v'$  [24]. This mimics the functional dependency  $h(\cdot) \not\perp h'(\cdot)$ , which means that a perturbation in function  $h(\cdot)$  will not affect the solution space of function  $h'(\cdot)$ ;  $\text{An}_g = \{v | (v \rightarrow \dots \rightarrow g) \in \mathcal{G}\}$ , denoting the ancestor nodes of  $g$  with a directed path starting at the ancestor node and ending at  $g$ . The corresponding graph with  $d = \{\emptyset, d_2, d_3, d_4\}$  will have the edge  $(y_i \rightarrow g)$  removed, while  $g \not\perp y_1$  still holds.

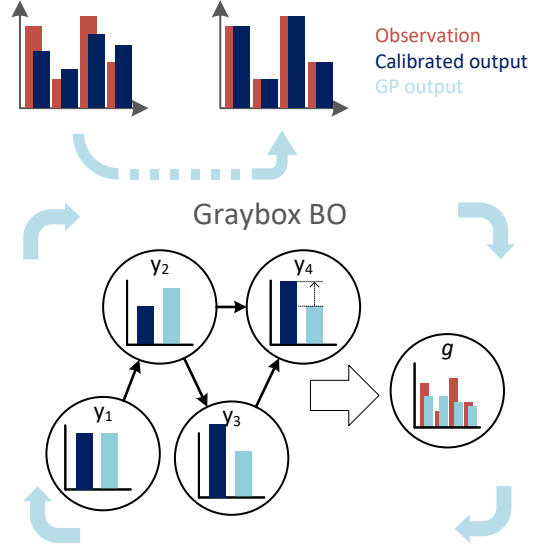


Fig. 3: Schematic illustration of the model calibration workflow based on graybox BO, where we leverage expert knowledge about functional dependency and metric function.

Moreover, it is reasonable to assume that the approximation of the computer model's output  $\{\eta_1(x), \dots, \eta_4(x)\}$  by the four GPs varies in computational complexity. The reason is that the complexities of the chosen function forms of  $\{\eta_1, \dots, \eta_4\}$  are different. Therefore, some GPs may need more queried data from the computer model than others. Taking into account of the decomposable structure of  $P_n(\mathbf{y}(x))$ , we extend the graybox acquisition function by *decoupled* decision-making and define the acquisition function as:

$$\begin{aligned} \alpha_n(x, \mathbf{z}) &:= \frac{1}{\mathbf{1}^\top \mathbf{z}} \mathbb{E}_{P_n(\mathbf{y}(x))} [u_{n+1}^*(\mathbf{z}, \mathbf{y}(x))] - u_n^* \\ u_{n+1}^*(\mathbf{z}, \mathbf{y}(x)) &:= \max_{x'} \mathbb{E}_{P_{n+1}(\mathbf{y}'(x'); \mathbf{z}, \mathbf{y}(x))} [g(\mathbf{y}')] \end{aligned} \quad (9)$$

where  $\mathbf{z} \in \{0, 1\}^4$  and  $P_{n+1}(\mathbf{y}'(x'); \mathbf{z}, \mathbf{y}(x))$  is defined as:

$$\prod_{i=1}^4 P_{n+1}(y'_i(x', Pa'_i); y_i(x, Pa_i))^{z_i} P_n(y'_i(x', Pa'_i))^{1-z_i}. \quad (10)$$

New candidates  $x^{n+1}$  is found by  $\text{argmax}_{x,z} \alpha_n(x, z)$ . When  $\mathbf{z} = \mathbf{1}$ ,  $P_{n+1}(\mathbf{y}'(x'); \mathbf{z}, \mathbf{y}(x)) = P_{n+1}(\mathbf{y}'(x'); \mathbf{y}(x))$ . The proposed objective can be seen as a generalization of the KG objective, which measures expected improvement when GPs are conditioned on predicted data  $(\mathbf{y}(x), x)$ . Here we further accommodate the case when a subset of GPs is conditioned on predicted data. Thus, candidates  $x^{n+1}$  with higher expected improvement can be expected by the proposed objective. Convergence analysis of graybox BO using our proposed acquisition function is provided in the appendix.

Due to the combinatorial nature of  $\mathbf{z}$ , it is hard to optimize w.r.t.  $\mathbf{z}$  directly. The most naive approach is to optimize  $\alpha_n$

w.r.t.  $x$  under every possible choice of  $\mathbf{z}$ , and the resulting computational cost is  $2^{|\mathbf{z}|}$  times that of the non-decoupled version. For the SIQR model in this paper,  $|\mathbf{z}| = 4$  and the increased cost is acceptable. Besides, the non-decoupled version is just a special case of the decoupled version, where  $\mathbf{z} = \mathbf{1}$ . Therefore, we can accelerate the computation by selecting a subset. In this paper, we choose  $\{(\mathbf{z} : z_1 = 1, z_{\neq 1} = 0), \dots, (\mathbf{z} : z_{|\mathbf{z}|} = 1, z_{\neq |\mathbf{z}|} = 0)\} \cup \{\mathbf{z} = \mathbf{1}\}$ , resulting  $|\mathbf{z}| + 1$  times the computational cost of the non-decoupled version.

---

#### Algorithm 1 Model Calibration Workflow

---

**Require:** Number of iteration  $N$ , Computer model  $\eta(x)$   
 $(X, Y) \leftarrow (X_{init}, \{\eta(x)\}_{x \in X_{init}})$  //  $X_{init}$  is a randomly initialized set of calibration parameter vectors.  
**for**  $n = \{0, \dots, N - 1\}$  **do**  
 $\mathcal{D}^n \leftarrow (X, Y)$   
 $P_n(y_i(x)) \leftarrow \mathcal{N}(\mu_n^i(x), \sigma_n^i(x))$   
 $x^{n+1} \leftarrow \operatorname{argmax}_x \hat{\alpha}_n(x)$   
 $(X, Y) \leftarrow X \cup \{x^{n+1}\}, Y \cup \{\eta(x^{n+1})\}$   
**end for**  
**return**  $x^{best} \leftarrow \operatorname{argmax}_x \hat{u}_N(x)$

---

#### IV. EXPERIMENTAL RESULTS OF SIMULATED DATASETS

In this section, we conduct experiments to evaluate and compare the performances of model calibration using various Bayesian Optimization (BO) methods<sup>2</sup>. We consider different setups of observed epidemiological data generated from simulated ‘‘ground-truth’’ models. In our experiments, both the ground-truth model  $\zeta$  and the computer model to calibrate  $\eta$  are SIQR models. Once a trial of epidemiological data  $\mathbf{d}$  is simulated, the ground-truth model is no longer accessible. It is also assumed that we are only accessible to computer models’ outputs. The goal is to validate the effectiveness of our graybox BO methods for model calibration in *expensive* scenarios and investigate how our proposed acquisition functions can improve the performance of graybox BO-based model calibration.

To generate data based on the ground-truth SIQR model  $\zeta$ , we set  $\beta^*(t) = 0.9I(t)$ ,  $\lambda^*(t) = 0.1I(t)$ ,  $\delta^* = 0.2$ ,  $\gamma^* = 0.2$ . The model to calibrate,  $\eta$ , takes the same form with undetermined parameters  $x$ , that is,  $\lambda(t, x) = x_1I(t)$ ,  $\beta(t, x) = x_2I(t)$ ,  $\delta = x_3$ , and  $\gamma = x_4$ . The initial conditions for both  $\zeta$  and  $\eta$  are:  $S(0) = 0.99 * N$ ,  $I(0) = 0.01 * N$ ,  $R(0) = 0$  and  $Q(0) = 0$ . We consider two scenarios representing the gap between the ground-truth model and the computer model to calibrate. The first way is to add noise to the ground-truth observations  $\mathbf{d}$ . The second is to have different setups of  $\eta$  from those of  $\zeta$ . In our experiments, we set  $\lambda^*(t)$  in  $\zeta$  as a non-linear function, that is,  $\lambda^*(t) = \log([I(t), S(t), R(t)]^\top [0.3, 0.06, 0.12] + 1)I(t)$ , while  $\lambda(t)$  in  $\eta$  still takes the linear form mentioned above. The corresponding plots for the 30-day simulations are shown in Figure 4.

<sup>2</sup>Code is available at [github.com/niuuhua1234/Epi-KG](https://github.com/niuuhua1234/Epi-KG).

We compare calibration performances based on the following BO methods: (i) the standard *Expected Improvement (EI)* in the blackbox BO framework without integrating functional structures, (ii) the standard *Knowledge Gradient (KG)*, (iii) the *Knowledge Gradient with composite function (KG-CF)*, (iv) *Knowledge Gradient with function network (KG-FN)*, and (v) the *Decoupled Knowledge Gradient with composite function (DG-CF)*. All algorithms have been implemented based on the BOTorch package [7] while the latter three are all graybox BO variants. In all our experiments, we have run each calibration method five times from the different random seeds, where each run starts with an initial dataset from the computer model,  $\mathcal{D}_0 = \{(\hat{y}^l = \eta(x^l), x^l)\}_{l=1}^{2^{D+1}}$ , where  $x^l$  is randomly selected in  $[0, 1]^D$ .

Experiments under all three ground-truth models are performed in complete-observation and incomplete-observation setups. In the latter setup, observations of compartment ‘S’ are assumed to be unknown, so  $d_1$  is not involved with the calibration procedure. This helps to investigate whether the function network organization of GPs allows more reliable model calibration under incomplete (decoupled) observation data  $\mathbf{d}$  by leveraging the ground-truth functional dependency.

##### A. Complete Observations

The experimental results under the complete-observation setting are shown in Figure 5. In all these experiments, it can be observed that our graybox BO methods, including KG-CF, perform significantly better than the blackbox BO methods, EI and KG. This demonstrates that integrating knowledge of  $g$  does help improve the calibration performance. The performance of KG-FN is slightly worse than KG-CF. This phenomenon can be ascribed to the following reasons. With complete observations, all the updating of GPs,  $\{y_1, \dots, y_4\}$  that approximate  $\{\eta_1, \dots, \eta_4\}$  are well-informed, making the information propagating via introducing statistical dependency less important. Besides, the function network organization of GPs make the acquisition estimator  $\hat{\alpha}$  more challenging to calculate reliably. As shown in (7), inputs of each GP include not only  $x$  but also random samples of  $Pa$ , which makes the estimated  $\hat{\alpha}$  unstable due to the stochastic nature of inputs, and consequently increases the difficulty of finding the optimal point of  $\hat{\alpha}(x)$  in each BO iteration. Last but not least, our proposed DG-CF performs better than KG-CF. This validates that the decoupled acquisition can better inform decision-making by conditioning on the predicted data of a subset of GPs, rather than the whole set of GPs.

##### B. Incomplete Observations

The experimental results under the incomplete-observation setting are shown in Figure 6. Again, our graybox BO methods perform significantly better than the blackbox BO methods. It should be noted that KG-FN can outperform KG-CF when the observations are noisy. This shows that integrating functional dependency does help to inform the calibration process, while the performance gain is not significant due to the accompanied optimization difficulty that we mentioned above. Finally, our

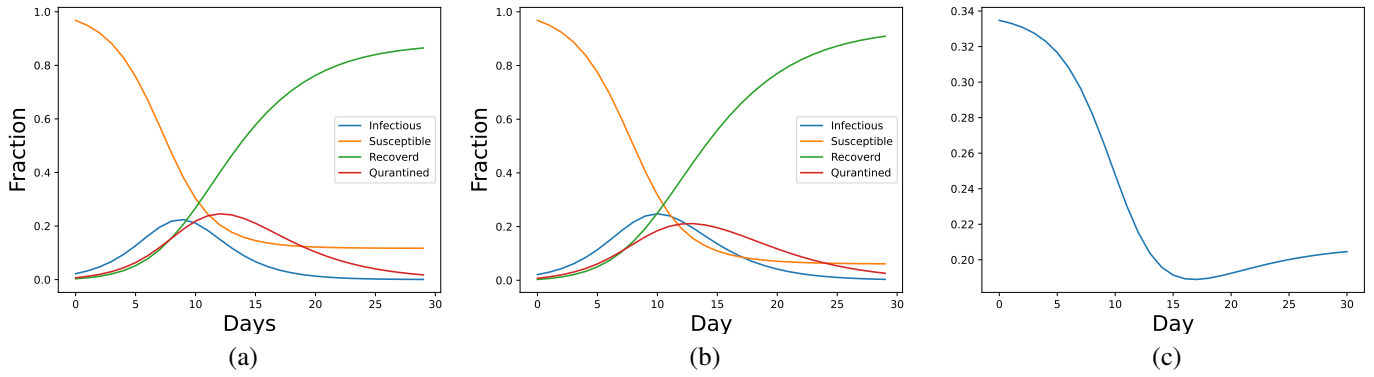


Fig. 4: The simulated ground-truth population fraction trajectories of each compartment for 30 days. (a) Trajectories from a SIQR model with linear derivative functions. (b) Trajectories corresponding to the case when derivation function  $\lambda^*(t)$  is non-linear. (c) The trajectory of  $\lambda^*(t)$  when it is set to be non-linear.

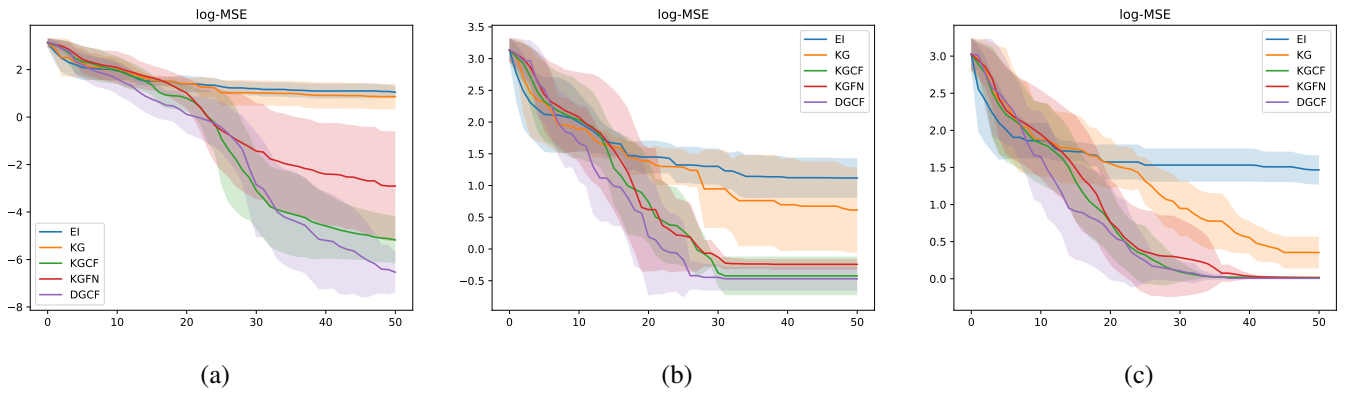


Fig. 5: Calibration performance. The logarithm of the MSE is shown with respect to the number of BO iterations. For the  $n_{th}$  iteration, the MSE is computed as  $-\sum_t f^t(x)$ , where  $x = \operatorname{argmax}_x \hat{u}_n(x)$ . Solid lines show the mean values of five runs and the shaded regions correspond to the standard deviations around the means. (a) Performance for a linear SIQR model  $\zeta$ . (b) Performance for a linear  $\zeta$  in the presence of noise. (c) Performance for a non-linear  $\zeta$ .

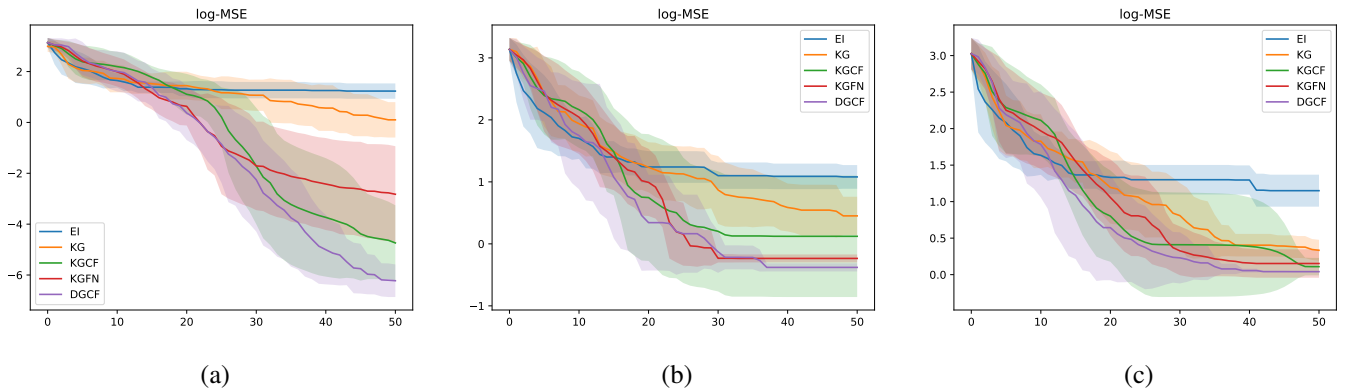


Fig. 6: Calibration performance runs under incomplete observations. (a) Performance for a linear SIQR model  $\zeta$ . (b) Performance for a linear  $\zeta$  in the presence of noise. (c) Performance for a non-linear  $\zeta$ . In all cases, we assume that the ground-truth trajectories of the susceptible population (compartment ‘S’) are missing.

proposed DG-CF performs better than KG-CF, validating again the advantages of the decoupled acquisition function.

In Figure 7, we also visualize population fraction trajectories generated from the computer models under the calibrated parameters derived by all methods in the setting with noisy and

incomplete observations from a linear SIQR model. It can be observed that all methods can provide non-trivial calibration results, showing that our BO-based calibration methods have a promising potential for epidemiological dynamic model calibration, when the computed model is *expensive*. Among

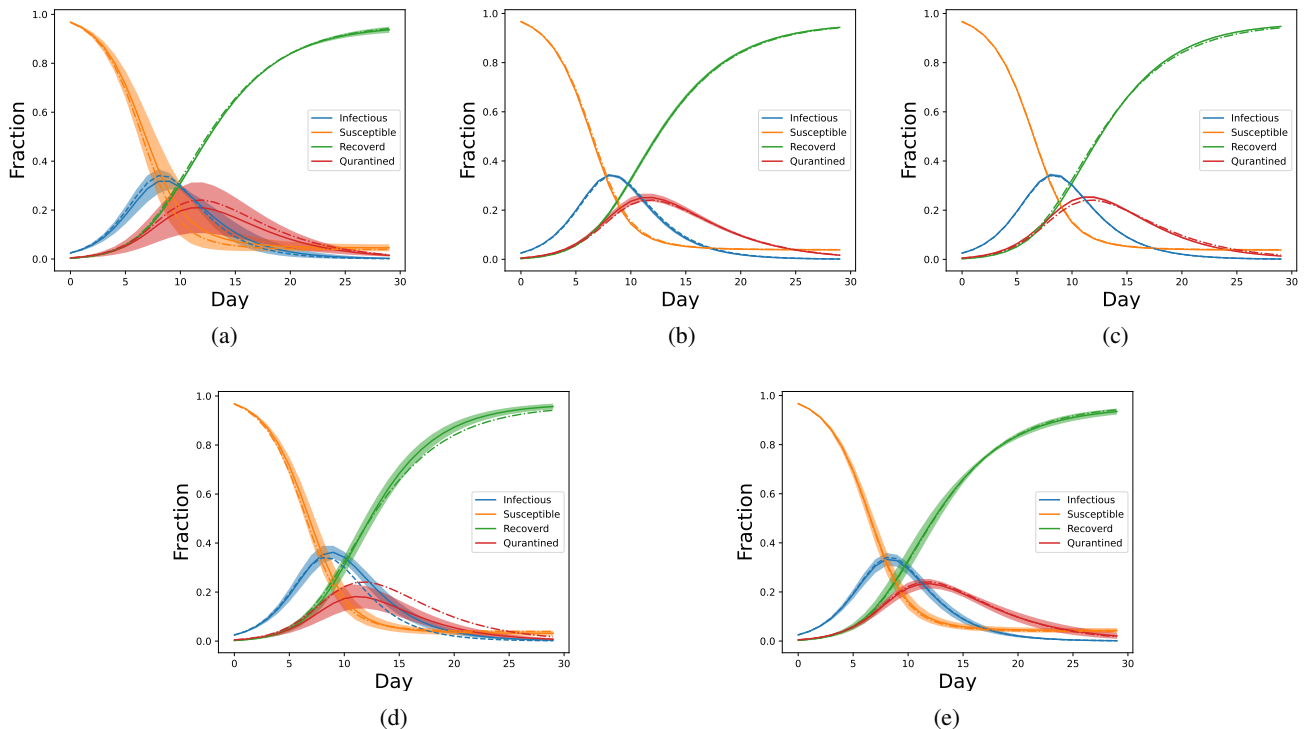


Fig. 7: Population fraction trajectories from the computer model  $\eta$  under the calibration parameters  $x^{best}$ , calibrated by (a) KG-CF, (b) KG-FN, (c) DG-CF, (d) EI, and (e) KG, with noisy observation from a linear  $\zeta$ . The solid lines represent the mean trajectories simulated from the corresponding calibrated computer models of five runs and the shaded regions illustrate the standard deviation intervals around the means. The dotted lines are the ground-truth population fraction trajectories.

all the BO variants, graybox BO variants KG-FN and DG-CF render the mean trajectories with smaller bias to the ground-truth ones as well as smaller variance, compared to KG-CF, EI, and KG. This again confirms that utilizing the functional structure and decoupled acquisition functions can help better inform decision-making during BO iterations.

## V. EXPERIMENTAL RESULTS OF REAL-WORLD DATASETS

To further confirm the effectiveness of our proposed methods in real-world scenarios, we apply them to calibrate the SIQR model  $\eta$  w.r.t. observe population trends during the COVID-19 pandemic. We use the data collected by the Johns Hopkins University Center for Systems Science and Engineering, via a R data package *covid19.analytics* [27]. We focus on the infectious populations of U.S. and U.K. For each country, there are 365 temporal observations of the infectious populations collected from June 1st, 2020, to June 1st, 2021.

We consider three variants of the SIQR models, denoted by  $\eta_S$ ,  $\eta_W$ , and  $\eta_{NN}$ . Calibrated Model  $\eta_S$  takes the same form as  $\eta$ , described in the previous experiment section. For model  $\eta_W$ ,  $\lambda(t)$  adopts a non-linear form,  $\lambda(t) = \log([I(t), S(t), R(t)]^\top [x_{1,1}, x_{1,2}, x_{1,3}] + 1)I(t)$ , while other components remain the same as that of  $\eta$ . Last but not least,  $\lambda(t)$  of model  $\eta_{NN}$  is set to be  $f_{NN}([I(t), S(t), R(t)]; x_{NN})I(t)$ . Here,  $f_{NN}$  is a neural network with parameters  $x_{NN}$  and three latent layers. The detailed information about the dimension and activation function in each layer of  $f_{NN}$  is summarized as follows: Input

Layer— $(3 \times 20, \text{Tanh})$ ; Output Layer— $(20 \times 1, \text{Sigmoid})$ ; Latent Layers— $\{(20 \times 20, \text{Tanh})\}_{i=1}^3$ ; The other components of  $\eta_{NN}$  follow those of  $\eta$ . This calibrated model setup is motivated by the common adoption of neural ODE for modeling the dynamics of complex systems, making it meaningful to validate proposed methods w.r.t. more flexible neural ODE models.

Unlike the simulated experiments, we know the initial state of each population and the total population. In the real-world scenarios, these values should be carefully selected. Since we only have the observations of the infectious population, the simplest choice is to set  $I(0)$  equal to the first-day's infectious observation, denoted by  $\hat{I}(0)$ ; and set the total population  $N$  to the population of each country. However, during the COVID-19 pandemic, most countries issued policies to discourage the spread of the disease. For example, people were suggested to work at home. The true total population that should be taken into account is much smaller than the population of each country. In light of the above reason and calibration quality, we set  $I(0) = x_5$  and  $N = x_6$  as two additional parameters in the calibrated model, and consider the ranges  $10^{-1}\hat{I}(0) \leq x_5 \leq 10\hat{I}(0)$  and  $10\hat{I}(0) \leq x_6 \leq 10^3\hat{I}(0)$ . In addition, the calibration of  $\eta_{NN}$  is divided into two stages. In the first stage, we calibrate  $\eta_S$  to the real-world observations. In the second stage, we replace  $\lambda(t) = x_1 I(t)$  by  $f_{NN}([S(t), Q(t), R(t)]; x_{NN})I(t)$ , obtaining an uncalibrated  $\eta_{NN}$ . Then, we adopt the adjoint gradient method [13] to compute gradients efficiently and stochastic

---

**Algorithm 2** Two-Stage Model Calibration Workflow

---

**Require:**  $N, \eta_{NN}(x), \eta_S(x)$   
 $x^{1st} \leftarrow \text{Algorithm-1}(N, \eta_S(x))$   
 $\{S(t), Q(t), R(t)\}_{t=0}^{T-1} \leftarrow \eta_S(x^{1st})$   
 $\mathcal{D} \leftarrow \{\hat{I}(t), S(t), Q(t), R(t)\}_{t=0}^{T-1}$   
 $x \leftarrow [x_{NN}, x_{2:6}^{1st}]$   
Optimize  $\eta_{NN}(x)$  w.r.t.  $x_{NN}; x_{2:6}^{1st}$  by stochastic gradient descent, based on  $\mathcal{D}$ , and obtain  $x^{2nd}$   
**return**  $x^{2nd}$

---

gradient descent to optimize parameters of  $f_{NN}(\cdot; x_{NN})$  and  $[\beta(t, x_2), \delta(t, x_3), \gamma(t, x_4)]$ . Values of  $x_{NN}$  are randomly initialized, and values of  $x_{2:6}$  found in the first stage are used as the initial values for the second stage. The batch size, the number of total iterations, the learning rate are set to 30, 2000 and  $5 \times 10^{-4}$ . The reason for this two-stage calibration is as follows. First, it should be noted that the goal of model calibration is to efficiently identify the value of key parameters rather than the optimization of all parameters. Compared to the parameters of  $f_{NN}$ , which collectively govern the  $\lambda(t)$ ,  $x_{2:6}$  act as hyper-parameters, each of which controls an individual component of the SIQR model. Therefore, properly setting the values or ranges  $x_{2:6}$  is crucial for the calibration quality. Second, while neural ODEs are typically optimized by stochastic gradient descent, the optimization procedure requires *complete observations* of all population compartments, or the marginal formulation that only depends on the observed population compartments. To be more specific, we are required to randomly select a window  $[t_0, t_{29}] \subset [0, T]$  during optimization. Then  $\eta_{NN}$  is used to simulate sub-trajectories for this window, starting from the ground-truth observation  $(\hat{I}(t_0), \hat{S}(t_0), \hat{Q}(t_0), \hat{R}(t_0))$ . However, in our experiment, only  $\hat{I}(t_0)$  is known, making the stochastic gradient descent infeasible. Performing normal gradient descent usually leads to poor optimization performance, where we always simulate trajectories from  $(\hat{I}(0), N - \hat{I}(0), 0, 0)$ . Since we only care about the calibration w.r.t. the infectious observations, a preferable choice is to use  $(\hat{I}(t_0), S(t_0), Q(t_0), R(t_0))$ , where  $S(t_0), Q(t_0), R(t_0)$  are simulated from  $\eta_S$ . The corresponding calibration workflow is presented in Algorithm 2.

Method	US ( $\times 10^6$ ↓)	UK ( $\times 10^4$ ↓)
KGCF	11.3087 ± 2.6014	44.6875 ± 4.1894
KGFN	8.0117 ± 0.5123	45.0617 ± 3.6110

TABLE I: The mean and standard deviation of the smallest MSEs achieved by KG-CF and KG-FN on the U.S. and U.K. COVID-19 datasets, from five model calibration runs with randomly initialized  $\mathcal{D}_0$ .

In Figures 8 and 9, we visualize the comparison of predicted trajectories from the three types of computer models, calibrated by KG-CF and KG-FN based on infectious observations of the U.S. and U.K. respectively. We note that, since only the infectious population compartment is observed, the DG-CF implementation is the same as KG-CF. From these figures,

all calibrated models by either KG-CF or KG-FN successfully capture the trends of the true observations. Compared to KG-CF, the calibration performances of KG-FN for all three model setups are generally better with lower variance as shown in Table I. With nonlinear  $\lambda(t)$ ,  $\eta_W$  fits better to the observations than  $\eta_S$ . Enhancing  $\lambda(t)$  by a neural network and applying the two-stage calibration process, the calibrated models emulate infection population curves that fit the observations better as expected. While the calibrated curves under all model setups exhibit single modes [25] due to the limited model expressiveness of the SIQR model family, the capability of our proposed calibration methods is well validated by multiple setups. It can be expected that calibrating more expressive models like ABMs [1]. will render better fitting to the true observations.

## VI. CONCLUSION & FUTURE WORK

In this work, we proposed epidemiological model calibration methods based on the BO framework. To improve calibration performance, we formulated the calibration problem as a customized graybox BO task, where expert knowledge about functional dependency and calibration performance metric function is integrated into the acquisition function. Furthermore, we proposed a decoupled acquisition function, which further exploits the decomposable nature of the functional structure. We conducted experiments using simulated data under three types of ground-truth models and two observation types to validate the model calibration performance of our proposed BO-based methods. Within a small number of BO iterations ( $\leq 50$ ), the proposed graybox BO methods can achieve good performance, leading to lower MSEs and faster convergence (in terms of BO iterations) compared to methods based on standard BO. To further confirm the capability of our methods to real-world problems, we calibrated three types of models to COVID-19 data. The experimental results demonstrate the efficacy of our BO-based methods for enabling the calibration of *expensive* computer models. While the experimental results show that utilizing ground-truth functional dependency can help the calibration process, the resulting formulation of the acquisition function can lead to optimization difficulties in practice, impairing the overall calibration performance. Thus, future work will focus on further investigation of the function network organization of GPs to achieve better performance. Besides, in the current work, the function network is limited to a single system, where each node corresponds to an element within that system. In a more general case, there can be multiple sub-systems interacting with one another, with each node in the network representing an entire sub-system. Our future investigation will consider extending the proposed calibration methods to accommodate this more general case. Finally, agent-based epidemiological models have a much larger number of critical parameters than compartmental models. Along with their significant computational complexity, the underlying functional dependency are also more complex, making their calibration tasks more challenging. Efficient

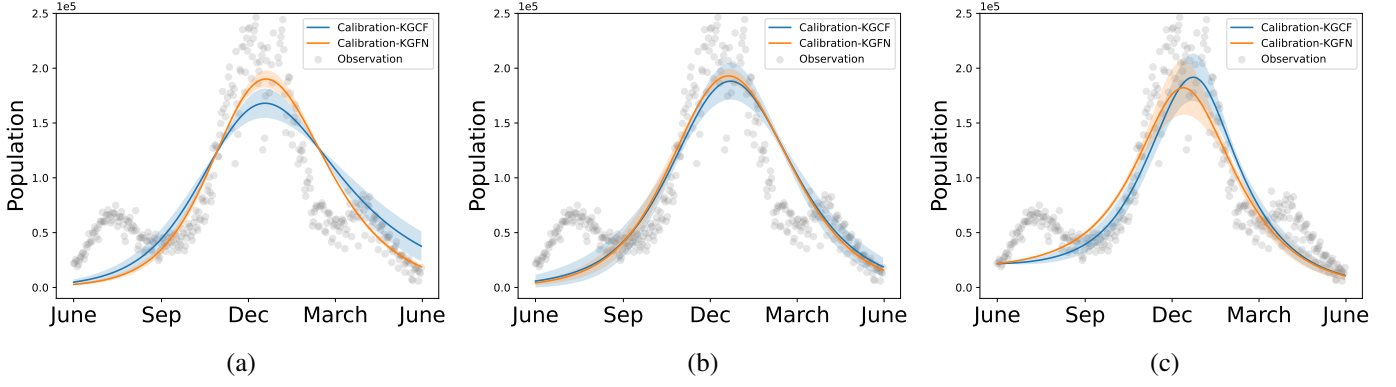


Fig. 8: Trajectories of the U.S. infectious population from the computer models (a)  $\eta_S$ , (b)  $\eta_W$ , and (c)  $\eta_{NN}$  under the calibrated parameters, calibrated by KG-CF and KG-FN. The solid lines represent the mean trajectories simulated from the corresponding calibrated computer models of five runs and the shaded regions illustrate the standard deviation intervals around the means. The scattered points are the ground-truth observations of the infectious population.

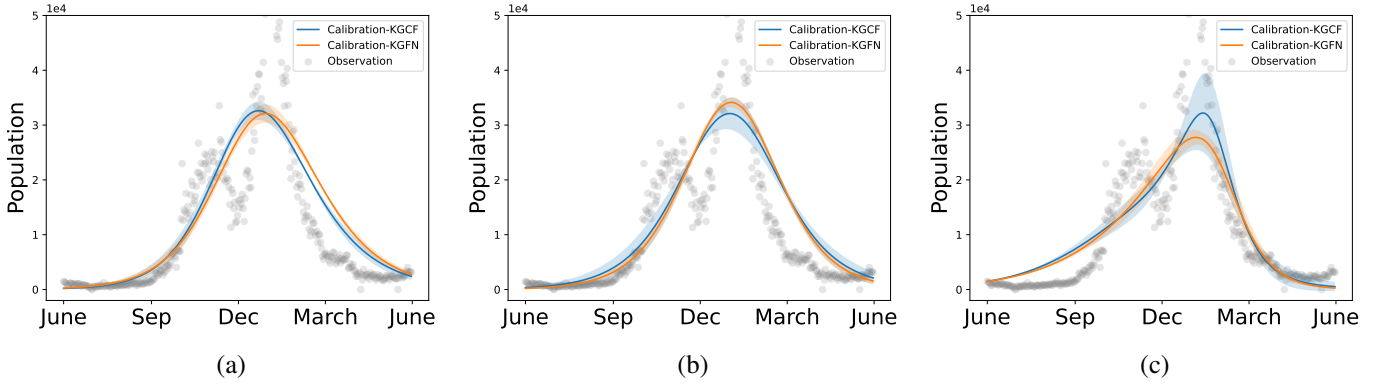


Fig. 9: Trajectories of the U.K. infectious population from the computer models (a)  $\eta_S$ , (b)  $\eta_W$ , and (c)  $\eta_{NN}$  under the calibrated parameters, calibrated by KG-CF and KG-FN. The solid lines represent the mean trajectories simulated from the corresponding calibrated computer models of five runs and the shaded regions illustrate the standard deviation intervals around the means. The scattered points are the ground-truth observations of infectious population.

calibration of ABMs for epidemiological modeling may require developing and validating different approximate solutions for BO acquisition functions, which remains an open problem for future research.

#### APPENDIX

We simplify the notations of  $\mathbb{E}_{P_n(y_i(x, Pa_i))}[\cdot]$  and  $\mathbb{E}_{P_n(Pa_i(x))}\mathbb{E}_{P_n(y_i(x, Pa_i))}[\cdot]$  as  $\mathbb{E}_n[\cdot]$  and  $\bar{\mathbb{E}}_n[\cdot]$  ( $\mathbb{E}_{n,(x, Pa_i)}[\cdot]$  and  $\bar{\mathbb{E}}_{n,x}[\cdot]$  to emphasize the dependency relationships). Accordingly,  $\mathbb{E}_{P_n(y_i(x, Pa_i))}[\mathbb{E}_{P_{n+1}(y'_i(x', Pa'_i)); y_i(x, Pa_i)}[\cdot]]$  and  $\mathbb{E}_{P_n(Pa_i(x))}\mathbb{E}_{n,(x, Pa_i)}[\mathbb{E}_{P_{n+1}(Pa'_i(x'))}\mathbb{E}_{n+1,(x', Pa'_i)}[\cdot]]$  can be denoted as  $\mathbb{E}_n[\mathbb{E}_{n+1}[\cdot]]$  and  $\bar{\mathbb{E}}_n[\bar{\mathbb{E}}_{n+1}[\cdot]]$ .

Both  $\mathbb{E}_n[g(y_i(x, Pa_i))]$  and  $\mathbb{E}_n[\max g(y_i)] (= \mathbb{E}_{n,x}[\max_{x'} g(y_i(x', Pa_i))])$  are martingales in that  $\mathbb{E}_n[\mathbb{E}_{n+1}[g(y'_i)]] = \mathbb{E}_{P_n(y'_i)}[g(y'_i)] = \mathbb{E}_n[g(y_i)]$ , and  $\mathbb{E}_n[\mathbb{E}_{n+1}[\max g(y_i)]] = \mathbb{E}_n[\max g(y_i)]$  by the law of total expectations [8], [20]. Furthermore,  $\bar{\mathbb{E}}[g(y_i)]$  and  $\bar{\mathbb{E}}[\max g(y_i)]$  are also martingales. The reason is as follows: Conditioning on  $Pa_i \sim P_n$ ,  $Pa'_i \sim P_{n+1}$  is independent of  $y_i \sim P_n$  as  $Pa_i$  is the common parent node within the

dependency structure  $y_i \leftarrow Pa_i \rightarrow Pa'_i$  [24]. Therefore,  $\bar{\mathbb{E}}_n[\bar{\mathbb{E}}_{n+1}[\cdot]] = \mathbb{E}_{P_n(Pa_i(x))}\mathbb{E}_{P_{n+1}(Pa'_i(x'))}[\bar{\mathbb{E}}_n\mathbb{E}_{n+1}[\cdot]] = \mathbb{E}_{P_n(Pa_i(x))}\mathbb{E}_{P_{n+1}(Pa'_i(x'))}\mathbb{E}_n[\cdot] = \bar{\mathbb{E}}_n[\cdot]$ .

**Lemma 1.** Let  $G_n^i(x) = \bar{\mathbb{E}}_{n,x}[\bar{\mathbb{E}}_{n+1}[g(y'_i(x', Pa'_i))] - \bar{\mathbb{E}}_n[g(y_i(x_*, Pa_i))]$ , where  $x_* = \operatorname{argmax}_x \bar{\mathbb{E}}_n[g(y_i(x, Pa_i))]$ , and  $x'_* = \operatorname{argmax}_{x'} \bar{\mathbb{E}}_{n+1}[g(y'_i(x', Pa'_i))]$ . Then  $G_n^i(x) \geq 0$ .

*Proof.* By definitions,  $\bar{\mathbb{E}}_{n+1}[g(y'_i(x_*, Pa'_i))] \leq \bar{\mathbb{E}}_{n+1}[g(y'_i(x'_*, Pa'_i))]$ . Thus,  $0 = \bar{\mathbb{E}}_n[\bar{\mathbb{E}}_{n+1}[g(y'_i(x_*, Pa'_i))] - \bar{\mathbb{E}}_n[g(y_i(x_*, Pa_i))] \leq G_n^i(x)$ .  $\square$

According to the definition of  $G_n^i(x)$ , we further define  $H_n^i = \mathbb{E}_{n,x_*}[\max g(y_i)] - \mathbb{E}_n[g(y_i(x_*, Pa_i))]$ , where  $x_* = \operatorname{argmax}_x \bar{\mathbb{E}}_n[g(y_i(x, Pa_i))]$ . We also denote  $J_n(x) = \mathbb{E}_{n,x}[H_{n+1}]$ . It can be observed that  $H_n^i \geq 0$  and  $J_n^i(x) \geq 0$ . Since  $\mathbb{E}_n[\max g(y_i)]$  is a martingale,  $H_n^i - J_n^i(x) = \mathbb{E}_{n,x}[\max \mathbb{E}_{n+1}[g(y'_i)]] - \max \mathbb{E}_n[y_i] = G_n^i(x)$ .

**Assumption 1.** We make the following assumptions:

- $x \in \mathbb{X}$  and  $\mathbb{X}$  is a compact metric space (e.g.  $(\mathbb{R}^n, \|\cdot\|_2)$ ) and the sample path of  $y_{i \in \{1, \dots, 4\}}$  is continuous.

- $\eta$  is in the state space of  $\mathbf{y} \sim P_n$  for  $n \geq 1$ .

**Lemma 2** (Lemma B.3 in [6]). *Supposing Assumption 1 holds and taking  $n \rightarrow \infty$ , then  $m_n^i$  converge to some  $m_\infty^i$  almost surely (a.s.) and uniformly on  $\mathbb{X}$ , and  $\sigma_n^i$  converges to some  $\sigma_\infty^i$  a.s., and uniformly on  $\mathbb{X} \times \mathbb{X}$ .*

**Theorem 1.** *Supposing Assumption 1 holds and taking  $n \rightarrow \infty$ , the decoupled acquisition function  $\alpha_n(x)$  converge to 0 a.s..*

*Proof.* First of all, it is clear that  $G_n^i$  and  $H_n^i$  are both continuous w.r.t.  $P_n$  and  $P_{n+1}$ . Thus, by Lemma 2,  $G_n \rightarrow G_\infty$  and  $H_n \rightarrow H_\infty$  when  $P_n \rightarrow P_\infty$ .

Denoting  $K^i = H_n^i - H_{n+1}^i$ , we have  $\bar{\mathbb{E}}_{n,x}[K_n^i] = H_n^i - J_n^i(x) = G_n^i(x)$ . By the assumption of  $\eta$ , we construct  $G_n$  based on a sample trajectory  $\{\eta^l(x^l), x^l\}_l^n$  and have:

$$\begin{aligned} \sum_{n=0}^{N-1} \bar{\mathbb{E}}_{1:n,x^{1:n}}[G_n^i(x^{n+1})] &= \sum_{n=0}^{N-1} \bar{\mathbb{E}}_{1:n+1,x^{1:n+1}}[K_n^i] \\ &= \bar{\mathbb{E}}_{1:N,x^{1:N}} \left[ \sum_{n=0}^{N-1} K_n^i \right] = H_0^i - \bar{\mathbb{E}}_{1:N,x^{1:N}}[H_N^i] \leq H_0^i < \infty, \end{aligned}$$

where  $P_0$  is generated from a given  $\mathcal{D}_0$ ,  $P_{n(\geq 1)}$  is generated from  $\mathcal{D}_0 \cup \{(y_l^i(x), x^l)\}_{l=1}^n$  with  $y_l^i(x) \sim P_l$ . Taking  $N \rightarrow \infty$ , we have  $\sum_{n=0}^{\infty} \mathbb{E}[G_n^i(x^{n+1})] \leq \infty$ . Since  $G_n^i(x) \geq 0$  by Lemma 1, the inequality implies  $G_\infty^i(x) = 0$  a.s..

By the definition of  $\alpha_n$ , we have  $\alpha_n(x) = \max_{\mathbf{z}, x} \frac{1}{1+\mathbf{z}} \sum_i (H_i - z_i J_n^i(x) - (1 - z_i) H_i) = \max_{\mathbf{z}, x} \frac{1}{1+\mathbf{z}} \sum_i z_i G_n^i(x)$ , and  $0 \leq \alpha_n(x^n) \leq \sum_i G_n^i(x^n)$ . Therefore,  $\lim_{n \rightarrow \infty} \alpha_n(x^n) = 0$  a.s..  $\square$

## REFERENCES

- [1] Alberto Aleta, David Martin-Corral, A Piontti, Marco Ajelli, Maria Litvinova, Matteo Chinazzi, et al. Modeling the impact of social distancing, testing, contact tracing and household quarantine on second-wave scenarios of the COVID-19 pandemic. *Publisher Full Text*, 2021.
- [2] Cleo Anastassopoulou, Lucia Russo, Athanasios Tsakris, and Constantinos Siettos. Data-based analysis, modelling and forecasting of the COVID-19 outbreak. *PLoS one*, 15(3):e0230405, 2020.
- [3] Christophe Andrieu, Nando De Freitas, Arnaud Doucet, and Michael I Jordan. An introduction to MCMC for machine learning. *Machine learning*, 50:5–43, 2003.
- [4] Rushil Anirudh, Jayaraman J Thiagarajan, Peer-Timo Bremer, Timothy Germann, Sara Del Valle, and Frederick Streit. Accurate calibration of agent-based epidemiological models with neural network surrogates. In *Workshop on Healthcare AI and COVID-19*, pages 54–62. PMLR, 2022.
- [5] Raul Astudillo and Peter Frazier. Bayesian optimization of composite functions. In *International Conference on Machine Learning*, pages 354–363. PMLR, 2019.
- [6] Raul Astudillo and Peter Frazier. Bayesian optimization of function networks. *Advances in neural information processing systems*, 34:14463–14475, 2021.
- [7] Maximilian Balandat, Brian Karrer, Daniel Jiang, Samuel Daulton, Ben Letham, Andrew G Wilson, and Eytan Bakshy. BOTorch: A framework for efficient Monte-Carlo Bayesian optimization. *Advances in neural information processing systems*, 33:21524–21538, 2020.
- [8] Julien Bect, François Bachoc, and David Ginsbourger. A supermartingale approach to Gaussian process based sequential design of experiments. 2019.
- [9] Soufiane Bentout, Abdennasser Chekroun, and Toshikazu Kuniya. Parameter estimation and prediction for coronavirus disease outbreak 2019 (COVID-19) in Algeria. *AIMS Public Health*, 7(2):306, 2020.
- [10] Walter E Beyeler, Erin Acquesta, Katherine A Klise, Monear Makvandi, and Patrick D Finley. Adaptive recovery model: Designing systems for testing tracing and vaccination to support COVID-19 recovery planning. Technical report, Sandia National Lab.(SNL-NM), Albuquerque, NM (United States), 2020.
- [11] Fred Brauer, Carlos Castillo-Chavez, Zhilan Feng, et al. *Mathematical models in epidemiology*, volume 32. Springer, 2019.
- [12] D Andrew Brown and Sez Atamturktur. Nonparametric functional calibration of computer models. *Statistica Sinica*, pages 721–742, 2018.
- [13] Ricky TQ Chen, Yulia Rubanova, Jesse Bettencourt, and David K Duvenaud. Neural ordinary differential equations. *Advances in neural information processing systems*, 31, 2018.
- [14] Dennis D Cox, Jeong-Soo Park, and Clifford E Singer. A statistical method for tuning a computer code to a data base. *Computational statistics & data analysis*, 37(1):77–92, 2001.
- [15] Peter I Frazier. Bayesian optimization. In *Recent advances in optimization and modeling of contemporary problems*, pages 255–278. Informa, 2018.
- [16] Peter I Frazier. A tutorial on Bayesian optimization. *arXiv preprint arXiv:1807.02811*, 2018.
- [17] Peter I Frazier, Warren B Powell, and Savas Dayanik. A knowledge-gradient policy for sequential information collection. *SIAM Journal on Control and Optimization*, 47(5):2410–2439, 2008.
- [18] Roman Garnett. *Bayesian optimization*. Cambridge University Press, 2023.
- [19] Sanmitra Ghosh, Paul Birrell, and Daniela De Angelis. Variational inference for nonlinear ordinary differential equations. In *International Conference on Artificial Intelligence and Statistics*, pages 2719–2727. PMLR, 2021.
- [20] Olav Kallenberg and Olav Kallenberg. *Foundations of modern probability*, volume 2. Springer, 1997.
- [21] George Em Karniadakis, Ioannis G Kevrekidis, Lu Lu, Paris Perdikaris, Sifan Wang, and Liu Yang. Physics-informed machine learning. *Nature Reviews Physics*, 3(6):422–440, 2021.
- [22] Marc C Kennedy and Anthony O’Hagan. Bayesian calibration of computer models. *Journal of the Royal Statistical Society: Series B (Statistical Methodology)*, 63(3):425–464, 2001.
- [23] Diederik P Kingma and Max Welling. Auto-encoding variational Bayes. *arXiv preprint arXiv:1312.6114*, 2013.
- [24] Daphne Koller and Nir Friedman. *Probabilistic graphical models: principles and techniques*. MIT press, 2009.
- [25] Takashi Odagaki. Exact properties of SIQR model for COVID-19. *Physica A: Statistical Mechanics and its Applications*, 564:125564, 2021.
- [26] Nicola Piovella. Analytical solution of SEIR model describing the free spread of the COVID-19 pandemic. *Chaos, Solitons & Fractals*, 140:110243, 2020.
- [27] Marcelo Ponce and Amit Sandhel. covid19.analytics: An r package to obtain, analyze and visualize data from the coronavirus disease pandemic. *Journal of Open Source Software*, 6(59), 2021.
- [28] Thomas J Santner, Brian J Williams, William I Notz, and Brain J Williams. *The design and analysis of computer experiments*, volume 1. Springer, 2003.
- [29] Khachik Sargsyan, Habib N Najm, and Roger Ghanem. On the statistical calibration of physical models. *International Journal of Chemical Kinetics*, 47(4):246–276, 2015.
- [30] Matthias Seeger. Gaussian processes for machine learning. *International journal of neural systems*, 14(02):69–106, 2004.
- [31] Chih-Li Sung and Ying Hung. Efficient calibration for imperfect epidemic models with applications to the analysis of COVID-19. *Journal of the Royal Statistical Society Series C: Applied Statistics*, 73(1):47–64, 2024.
- [32] Rui Tuo, Shiyuan He, Arash Pourhabib, Yu Ding, and Jianhua Z Huang. A Reproducing Kernel Hilbert Space approach to functional calibration of computer models. *Journal of the American Statistical Association*, 118(542):883–897, 2023.
- [33] Rui Tuo and CF Jeff Wu. A theoretical framework for calibration in computer models: Parametrization, estimation and convergence properties. *SIAM/ASA Journal on Uncertainty Quantification*, 4(1):767–795, 2016.
- [34] Rui Tuo and CF Jeff Wu. Efficient calibration for imperfect computer models. 2015.